High field exotic metal in a Kondo insulator

Ziji Xiang¹,* Lu Chen¹, Kuan-Wen Chen¹, Colin Tinsman¹, Yuki Sato²,

Tomoya Asaba^{1,3}, Helen Lu⁴, Yuichi Kasahara², Marcelo Jaime⁴, Fedor

Balakirev⁴, Fumitoshi Iga⁵, Yuji Matsuda², John Singleton⁴,[†] and Lu Li^{1‡}

¹Department of Physics, University of Michigan, Ann Arbor, MI 48109, USA

²Department of Physics, Kyoto University, Kyoto 606-8502, Japan

³MPA-Q, Los Alamos National Laboratory, Los Alamos, NM, USA

⁴National High Magnetic Field Laboratory (NHMFL), MS E536,

Los Alamos National Laboratory, Los Alamos, NM 87545

⁵Institute of Quantum Beam Science, Graduate School of Science and Engineering,

Ibaraki University, Mito 310-8512, Japan

(Dated: December 26, 2020)

^{*} zixiang@umich.edu

[†] jsingle@lanl.gov

[‡] luli@umich.edu

Within condensed matter systems, strong electronic interactions often lead to exotic quantum phases. One such phase occurs in the Kondo insulator YbB₁₂, the insulating state of which exhibits phenomena characteristic of metals, such as magnetic quantum oscillations [1], a gapless fermionic contribution to the heat capacity [2, 3], and itinerant-fermion thermal transport [3]. To understand these phenomena, it is informative to study their evolution as the energy gap of the Kondo-insulator state is closed by a large magnetic field. We show here that clear quantum oscillations are observed in the resulting high-field metallic state in YbB₁₂; this is despite it possessing a relatively high resistivity, very large effective masses and a huge Kadowaki-Woods ratio, a combination that normally precludes quantum oscillations. The quantum-oscillation frequency and the cyclotron mass both display a strong field dependence. By tracking the Fermi-surface area, we conclude that the same quasiparticle band gives rise to the quantum oscillations in both insulating and metallic states. These data are understood most simply using a two-fluid picture where unusual quasiparticles, contributing little or nothing to charge transport, coexist with conventional fermions. Our observations of the complex field-dependent behaviour of the exotic fermion ensemble inhabiting YbB₁₂ provide strong constraints for existing theoretical models.

In Kondo insulators (KIs), an energy gap is opened up by strong coupling between a lattice of localized moments and the extended electronic states. The resulting Kondo gap $E_{\rm g}$ is usually narrow (typically $E_{\rm g} \simeq 5-20$ meV), yet the rôle it plays in charge transport is more complicated than that of the bandgap in conventional semiconductors. A low-temperature (T) saturation of the resistivity has long been known in two prototypical KIs, ${\rm SmB_6}$ and ${\rm YbB_{12}}$ [4, 5]; both are mixed-valence compounds with strong f-d hybridization that defines the band structure close to the Fermi energy. While the saturation might suggest additional metallic conduction channels, the high resistivity value within the weakly T-dependent "plateau" implies that these are highly unconventional [1, 4]; one interpretation is the presence of topologically protected surface states [6].

Recently, magnetic quantum oscillations, suggestive of a Fermi surface (FS), and thus totally unexpected in an insulator, have been detected in both SmB_6 and YbB_{12} [1, 7–10]. Whilst some have attributed the oscillations in SmB_6 to residual flux [11], the flux-free growth process of YbB_{12} (see Methods) excludes such a contribution. The oscillations in YbB_{12} are observed in both the resistivity ρ (the Shubnikov-de Haas, SdH, effect) and the magnetization M (the de Haasvan Alphen, dHvA, effect) at applied magnetic fields H where the gap is still finite. The T-dependence of the oscillation amplitude follows the Lifshitz-Kosevich (LK) formula, which is

based on Fermi-liquid theory [1]. Moreover, a contribution from gapless quasiparticle excitations to the heat capacity C has been detected in both KIs [2, 3, 10]. Though the thermal-transport observations remain controversial in SmB₆ [10, 12, 13], YbB₁₂ shows a T-linear zero-field thermal conductivity κ_{xx} , a characteristic of itinerant fermions [3]. The agreement of the FS parameters derived from the quantum oscillations, heat capacity, and thermal conductivity in YbB₁₂ suggests that the same quasiparticle band is responsible [3].

Despite this apparent consistency, the mystery remains: how can itinerant fermions exist in a gapped insulator and transport heat but *not* charge? In response, many theoretical models entered the fray, including magnetoexcitons [14], Majorana fermions [15, 16], emergent fractionalized quasiparticles [17, 18] and non-Hermitian states [19]. As these scenarios frequently envisage some form of exotic in-gap states, it is potentially invaluable to observe how the properties of KIs evolve as the energy gap $E_{\rm g}$ closes.

The cubic rare-earth compound YbB₁₂ is an excellent platform on which to carry out such studies. In YbB₁₂, the Kondo gap ($E_g \approx 15 \text{ meV} [20]$) is closed by large H, leading to an insulator-to-metal (I-M) transition at fields ranging from $\mu_0 H_{\text{I-M}} \simeq 45\text{-}47\,\text{T}$ ($\mathbf{H} \parallel [100]$) to 55-59 T ($\mathbf{H} \parallel [110]$) [1, 21, 22]. As revealed by a large Sommerfeld coefficient γ of heat capacity [2], Kondo correlation does not break down at the I-M transition, remaining strong to 60 T and beyond in the high-field metallic state; hence, this can be termed a Kondo metal (KM) [23]. In this study, we apply both transport and thermodynamic measurements, including ρ , penetration depth, M, and dilatometry, to YbB₁₂. By resolving quantum oscillations and tracking their T and H dependence in the KM state, we trace the fate of the possible neutral quasiparticles at fields above the gap closure and expose their interactions with more conventional charged fermions.

In our YbB₁₂ samples, M and magnetostriction data show that the I-M transition occurs at $\mu_0 H_{\text{I-M}} = 46.3 \,\text{T}$ (**H** || [100]); the tiny valence increase of Yb ions at the transition suggested by magnetostriction reinforces the KM nature of the high-field metallic state (see Methods and Extended Data Fig. 1). To probe the electronic structure of the KM state, a proximity-detector-oscillator (PDO) was used (see Methods) for contactless SdH effect studies. The PDO technique is sensitive to the sample skin depth, providing a direct probe of changes in the conductivity of the metallic KM state. The setup illustrated in the inset of Fig. 1a was rotated on a cryogenic goniometer to achieve **H**-orientation-dependent measurements. Fig. 1a summarizes the H dependence of the PDO frequency f as **H** rotates from [100] to [110].

The low conductivity of the KI state suggests that the MHz oscillatory field from the PDO coil

will completely penetrate the sample [24]. Therefore, the response of the PDO is dominated by the sample skin depth only when the sample enters the KM state and the conductivity increases significantly (see Methods). The transition between these regimes is marked by a dip in the f versus H curves close to $H_{\rm I-M}$, above which magnetic quantum oscillations emerge. Fig. 1b displays Δf , the oscillatory component of f, at various angles θ as a function of 1/H. The distinct oscillation pattern observed for $\mathbf{H}||[100]$ ($\theta=0$) is preserved up to $\theta\approx 21^\circ$ (Fig. 1b), being strongly modified at higher angles (Extended Data Fig. 2a).

The oscillations in Δf represent a single series that is intrinsically aperiodic in 1/H; attempts to fit them using a superposition of conventional oscillation frequencies fail to reproduce the raw data (Supplementary Information). To demonstrate the point further, Fig. 1c compares Landau-level indexing plots for the low-field KI and high-field KM states, both with $\mathbf{H} \parallel [100]$. The oscillatory component of the resistivity $\Delta \rho$ in the KI state is shown in the inset of Fig. 1c and indexed conventionally using integers for minima and half integers for maxima in ρ . For the KM state, peaks in f correspond to peaks in conductivity [24], and are therefore indexed using integers [25]. A further subdivision of the oscillations, reminiscent of a second harmonic, is likely due to Zeeman splitting of the quasiparticle levels [25]; these features are marked with "+" and "-" assuming signs expected for conventional Zeeman shifts. In the KI state, the plot of Landau level index N versus 1/H is a straight line, as expected for a field-independent quantum oscillation frequency in a nonmagnetic system. By contrast, in the KM state the 1/H positions of the oscillations have a nonlinear relationship with N which we shall describe below. (Here we note that the magnetic induction $B \approx \mu_0 H$, since $\mu_0 H$ is large and YbB₁₂ has a weak magnetization; see Methods).

Nevertheless, despite their unusual periodicity, the *T*-dependences of individual oscillation amplitudes in the KM state (Fig. 1d) closely follow the LK formula [25],

$$\Delta f(T) \propto \frac{2\pi^2 k_{\rm B} T / E_{\rm c^*}}{\sinh(2\pi^2 k_{\rm B} T / E_{\rm c^*})},$$
 (1)

suggesting that they are almost certainly due to fermions. (Here, $k_{\rm B}$ is the Boltzmann constant and $E_{\rm c^*}$ the cyclotron energy). However, the derived value of $E_{\rm c^*}$ varies nonlinearly with H, indicating that the cyclotron mass $m^* = eB/E_{\rm c^*}$ is a function of H (Fig. 2c).

The relationship between oscillation indices and magnetic field is described empirically by

$$N + \lambda = \frac{F_0}{\mu_0 (H_N - H^*)},\tag{2}$$

where an offset field of $\mu_0 H^* = 41.6$ T has been subtracted from $\mu_0 H_N$. Here, λ is a phase factor, N is again the index, H_N is the field at which the corresponding feature (e.g., peak) occurs and F_0

is the slope. Eq. 2 is symptomatic of a FS pocket that progressively depopulates as H increases, for reasons that we will discuss below. In such cases, the Onsager relationship $F(B) = \frac{\hbar}{2\pi e}A(B)$ between the FS extremal cross-sectional area A and the frequency F of the corresponding quantum oscillations still applies even when A changes with H (see Methods). Since $B \approx \mu_0 H$, we write $B^* = \mu_0 H^*$ and represent the field dependence of Eq. 2 using a B-dependent frequency

$$F_{\rm KM}(B) = \frac{F_0}{B - B^*} B; \tag{3}$$

this is associated with a *B*-dependent extremal area $A(B) = \frac{A_0}{B - B^*} B$, where $A_0 = \frac{2\pi e}{\hbar} F_0$ [26].

Analyzed in these terms, our data indicate that the quantum oscillations seen in the KM state are due to a FS pocket that is the same as, or very closely related to, the FS pocket in the KI state which contributes quantum oscillations and a T-linear term in both C and κ_{xx} [2, 3]. This is strongly suggested by the field dependence of F_{KM} (Eq. 3) shown in Fig. 2b. Even a cursory inspection reveals that Eq. 3, describing oscillations in the KM state, gives a frequency close to that of the KI-state oscillations when extrapolated back to H_{I-M} . This is true for all angles θ at which oscillations were measured; using appropriate F_0 values (Extended Data Table 1) and substituting fields $B = \mu_0 H_{I-M}(\theta)$ on the phase boundary (minima in PDO data; Fig. 1a) into Eq. 3 gives the frequencies shown as magenta diamonds in the inset of Fig. 2b. The θ -dependence of $F_{KM}(\mu_0 H_{I-M})$ thus deduced tracks the behaviour of the dHvA frequencies measured in the KI state, albeit with an offset ≈ 100 T (Fig. 2b). This offset may be due to a discontinuous change in F at the phase boundary; however, it could also result from the potential uncertainty in determining the H-position of any phase transition associated with a valence change [28]. Substituting values of $\mu_0 H_{I-M}$ decreased by ≈ 0.8 T into Eq. 3 yields an exact match of F_{KM} with the quantum-oscillation frequencies observed in the KI state (Fig. 2b, inset).

Further evidence that the same FS pocket contributes to quantum oscillations in both the KI and the KM states comes from the cyclotron masses. As shown in Fig. 2c, a cyclotron mass $m^* \approx 7m_0$ (m_0 is the free electron mass) is deduced from the T-dependence of the quantum oscillations at fields just above and just below the I-M transition (m^* in the KI state is obtained from the dHvA oscillations, which we suggest to be more fundamental; see Methods.) As mentioned above, m^* in the KM state is enhanced by increasing field. This effect is also captured by the unusual field-dependent Zeeman splitting of the SdH peaks (Extended Data Fig. 2, inset). In Fig. 2d we plot the spin-splitting factor S [25] calculated from the SdH data (see Methods). The field enhancement of S generally tracks that of m^* , consistent with elementary expectations of Landau quantization

(Methods). The scaling yields a g-factor $g \approx 0.084$, much smaller than that for typical weakly-interacting electron systems($g \approx 2$) [25].

The consistency of the frequency and mass across the I-M phase boundary indicates that the novel quasiparticles detected in the KI state of YbB₁₂ [1], which are probably charge neutral [3], also cause the SdH effect in the KM state (see Methods for further discussion). The unusual nature of the KM state is further revealed by magnetotransport experiments. To reduce Joule heating as the KI state is traversed, we used a pulsed-current technique (see Methods). Current is only applied to the sample when $H > H_{\rm I-M}$, as sketched in the inset of Fig. 3a. Below 10 K, very weak longitudinal magnetoresistance (MR) is observed above 50 T (Extended Data Fig. 3) and is preserved up to \approx 68 T (Extended Data Fig. 2), permitting an analysis of the T-dependence of the resistivity ρ in the KM state. Fig. 3a and Fig. 3b show ρ at 55 T as a function of T and T^2 , respectively. The $\rho - T$ curve shows a maximum at $T^* = 14$ K. With decreasing T, a linear T-dependence develops below 9 K and extends down to $T \approx 4$ K; subsequently, a Fermi-liquid-like T^2 -behaviour is established below $T_{\rm FL} = 2.2$ K. The overall behaviour of $\rho(T)$ mimics that of a typical Kondo lattice where the Kondo coherence develops at T^* and a heavy Fermi-liquid state forms below $T_{\rm FL}$ [29]. The residual resistivity $\rho(T \to 0) \approx 0.34$ m Ω -cm indicates that the KM state may be classified as a "bad metal".

Owing to the relatively high resistivity in the KM state, the Kadowaki-Woods (KW) ratio A_2/γ^2 (A_2 is the T^2 -coefficient of resistivity) is surprisingly large. Using the value of A_2 obtained from the fit in Fig. 3b and the Sommerfeld coefficient given by the pulsed-field heat-capacity measurements ($\gamma \simeq 63 \text{ mJ mol}^{-1} \text{ K}^{-2}$ at 55 T [2], see Methods), the estimated KW ratio is $1.46 \times 10^{-2} \ \mu\Omega$ cm (K mol/mJ)², three and four orders of magnitude larger than typical values for heavy-fermion compounds and transition metals, respectively (Fig. 3c). Such an abnormal KW ratio cannot be addressed by the degree of degeneracy of the quasiparticles, which tends to suppress the KW ratio in many Yb-based systems [32, 33].

It should be clear that the fermions responsible for the high-field quantum oscillations cannot on their own account for the transport and thermal properties of the KM state. First, even if they were capable of carrying charge, their field-dependent SdH frequency and mass would yield strong magnetoresistance (see Methods); the negligible magnetoresistance observed suggests that an additional, much more effective conducting channel is present. Second, the FS pocket deduced from the SdH oscillations would only account for 4-5% of the observed γ (see Methods). Therefore, a separate FS of more conventional heavy fermions is *required* to account for the charge-transport

properties and the large Sommerfeld coefficient of the KM state. The heavy effective mass of these fermions (see Methods) and the relatively high T>0.5 K used for our measurements would prevent their quantum oscillations being seen, even in a very clean system (a combination of dilution refrigerator and pulsed magnet is under long-term development to overcome such challenges). The "bad-metal" properties the KM state, indicative of low charge carrier mobilities and thus provide additional impediments for the observation of quantum oscillations, giving further support to the idea that the SdH effect is due to unconventional quasiparticles which are distinct from the heavy electrons.

Our results imply an intriguing two-fluid picture in YbB₁₂ that includes (i) a FS pocket of quasiparticles obeying Fermi-Dirac statistics but contributing little to the transport of charge; and (ii) more conventional charged fermions. For brevity, we refer to (i) as neutral fermions (NFs). These NFs cause quantum oscillations in both KI and KM states, whereas (ii) dominate the electrical transport properties and the low-T heat capacity in the KM state. Under this two-fluid description, the I-M transition produces a sudden increase of the density of (ii), which changes from a thermally excited low-density electron gas in the KI state to a dense liquid of heavy, charged quasiparticles in the KM state. As a result, when H increases past H_{I-M} , the much enhanced number of states available close to the Fermi energy will act as a "reservoir" into which quasiparticles from the NF FS can scatter or transfer (for analogous situations in other materials, see [34, 35]). In this sense, the falling quantum-oscillation frequency parameterized by Eq. 3 can be interpreted an indication that the NF FS becomes less energetically favourable in the KM state; the availability of the KM "reservoir" means that quasiparticles can transfer out and thus be depopulated. As the NF FS shrinks, the effective mass increases (Fig. 2c), possibly due to nonparabolicity of the corresponding band and/or field-induced modification of the bandwidth or interactions contributing to the effective mass renormalization [36]. Also, the fact that the quantum oscillations caused by the NF FS are strongly affected by the I-M transition (i.e., the frequency becomes H dependent and Zeeman splitting becomes evident in the KM state) shows that they are an intrinsic property of YbB₁₂, laying to rest suggestions that they are caused by a minority phase (c.f. the Al flux proposal for SmB₆ [11]) or surface effect.

The survival of the NFs above the gap closure and their coexistence with charged excitations in a Fermi-liquid-like state [17, 37, 38] leads to an interesting scenario; in such a state, Luttinger's theorem may be violated and a continuous variation of FS properties is allowed [38]. In addition, the interaction of a relatively conventional FS with an ensemble of quasiparticles unable to

transport charge is a feasible prerequisite for ρ varying linearly with T (Fig. 3a) [39]. We stress here that the continuous evolution of both the FS size and cyclotron mass, the small g-factor and the interactions with more conventional charge carriers are unusual characteristics of the NFs that should be addressed by future theoretical works.

Finally, the scaling behaviour between the magnetization and the B-dependence of orbit area (see Supplementary Information), as well as the large "offset" field H^* needed to linearize the Landau diagrams (Fig. 2a), may suggest underlying nontrivial magnetic properties in the KM state. Indeed, H^* bears a qualitative similarity to the gauge field [40] in the composite-fermion interpretation of the two-dimensional fractional quantum Hall effect (FQHE). Whether this similarity is coincidental, however, is still an open question. In three-dimensional materials, an emergent gauge field, which can be felt by the charge carriers and manifest itself in transverse transport measurements, might originate from chiral spin textures in a skyrmion lattice phase [41]. Nevertheless, such a topologically nontrivial magnetic structure has not yet been proposed for YbB₁₂ and the potential physical significance of H^* awaits further investigation.

DATA AVAILABILITY

The data that support the plots within this paper and other findings of this study are available from the corresponding authors upon reasonable request.

CODE AVAILABILITY

The code that support the plots within this paper and other findings of this study are available from the corresponding authors upon reasonable request.

ACKNOWLEDGEMENTS

We thank Lin Jiao, Liang Fu, Senthil Todadri, Tom Lancaster, Paul Goddard, Hiroshi Kontani, Hiroaki Shishido and Robert Peters for discussions. This work is supported by the National Science Foundation under Award No. DMR-1707620 and No. DMR-2004288 (transport measurements), by the Department of Energy under Award No. DE-SC0020184 (magnetization measurements), by the Office of Naval Research through DURIP Award No. N00014-

17-1-2357 (instrumentation), and by Grants-in-Aid for Scientific Research (KAKENHI) (Nos. JP15H02106, JP18H01177, JP18H01178, JP18H01180, JP18H05227, JP19H00649, JP20H02600 and JP20H05159) and on Innovative Areas "Quantum Liquid Crystals" (No. JP19H05824) from Japan Society for the Promotion of Science (JSPS), and JST CREST (JPMJCR19T5). A major portion of this work was performed at the National High Magnetic Field Laboratory, which is supported by National Science Foundation Cooperative Agreement No. DMR-1644779 and the Department of Energy (DOE). J.S. and M.J. thank the DOE for support from the BES program "Science in 100 T". The experiment in NHMFL is funded in part by a QuantEmX grant from ICAM and the Gordon and Betty Moore Foundation through Grant GBMF5305 to Dr. Ziji Xiang, Tomoya Asaba, Lu Chen, Colin Tinsman, and Dr. Lu Li. We are grateful for the assistance of You Lai, Doan Nguyen, Xiaxin Ding, Vivien Zapf, Laurel Winter, Ross McDonald and Jonathan Betts of the NHMFL.

AUTHOR CONTRIBUTIONS

F.I. grew the high-quality single crystalline samples. Z.X., L.C., K-W.C., C.T., Y.S., T.A., H.L., F.B., J.S. and L.L. performed the pulsed field PDO and resistivity measurements. Z.X., T.A. and J.S. performed the pulsed field magnetometry measurements. L.C., C.T. and M.J. performed the pulsed field magnetostriction measurements. Z.X., K-W.C., Y.K., Y.M., J.S. and L.L. analyzed the data. Z.X., Y.M., J.S. and L.L. prepared the manuscript.

AUTHOR INFORMATION

The current address of M.J. is Physikalisch-Technische Bundesanstalt, Braunschweig 38116, Germany. The authors declare no competing financial interests. Correspondence and requests for materials should be addressed to Z.X.(zixiang@umich.edu), J.S.(jsingle@lanl.gov) and L.L.(luli@umich.edu).

^[1] Xiang, Z. et al. Quantum oscillations of electrical resistivity in an insulator. Science 362, 65-69 (2018).

^[2] Terashima, T. T., Matsuda, Y. H., Kohama, Y., Ikeda, A., Kondo, A., Kindo, K. & Iga, F. Magnetic-field-induced Kondo metal realized in YbB₁₂. *Phys. Rev. Lett.* **120**, 257206 (2018).

- [3] Sato, Y. *et al.* Unconventional thermal metallic state of charge neutral fermions in an insulator. *Nat. Phys.* **15**, 954 (2019).
- [4] Cooley, J. C., Aronson, M. C., Fisk, Z. & Canfield, P. C. SmB₆: Kondo insulator or exotic metal? *Phys. Rev. Lett.* **74**, 1629 (1995).
- [5] Kasaya, M., Iga, F., Takigawa, M. & Kasuya, T. Mixed valence properties of YbB₁₂. J. Magn. Magn. Mater. 47&48, 429-435 (1985).
- [6] Dzero, M., Sun, K., Galitski, V. & Coleman, P. Topological Kondo insulators. *Phys. Rev. Lett.* **104**, 106408 (2010).
- [7] Li, G. et al. Two-dimensional Fermi surfaces in Kondo insulator SmB₆. Science **346**, 1208-1212 (2014).
- [8] Tan, B. S. et al. Unconventional Fermi surface in an insulating state. Science 349, 287-290 (2015).
- [9] Xiang, Z. *et al.* Bulk rotational symmetry breaking in Kondo insulator SmB₆. *Physical Review X* **7**, 031054 (2017).
- [10] Hartstein, M. *et al.* Fermi surface in the absence of a Fermi liquid in the Kondo insulator SmB₆. *Nat. Phys.* **14**, 166-172 (2018).
- [11] Thomas, S. M., Ding, X., Ronning, F., Zapf, V., Thompson, J. D., Fisk, Z., Xia, J. & Rosa, P. F. S. Quantum oscillations in flux-grown SmB₆ with embedded aluminum. *Phys. Rev. Lett.* **122**, 166401 (2019).
- [12] Xu, Y., Cui, S., Dong, J. K., Zhao, D., Wu, T., Chen, X. H., Sun, K., Yao, H. & Li, S. Y. Bulk fermi surface of charge-neutral excitations in SmB₆ or not: a heat-transport study. *Phys. Rev. Lett.* **116**, 246403 (2016).
- [13] Boulanger, M-E. *et al.* Field-dependent heat transport in the Kondo insulator SmB₆: phonons scattered by magnetic impurities. *Phys. Rev. B* **97** 245141 (2018).
- [14] Knolle, J. & Cooper, N. R. Excitons in topological Kondo insulators: Theory of thermodynamic and transport anomalies in SmB₆. *Phys. Rev. Lett.* **118**, 096604 (2017).
- [15] Erten, O., Chang, P.-Y., Coleman, P. & Tsvelik, A. M. Skyrme insulators: Insulators at the brink of superconductivity. *Phys. Rev. Lett.* **119**, 057603 (2017).
- [16] Varma, C. M. Majoranas in mixed-valence insulators. Phys. Rev. B 102, 155145 (2020).
- [17] Chowdhury, D., Sodemann, I. & Senthil, T. Mixed-valence insulators with neutral Fermi-surfaces. *Nat. Commun.* **9**, 1766 (2018).

- [18] Sodemann, I., Chowdhury, D. & Senthil, T. Quantum oscillations in insulators with neutral Fermi surfaces. *Phys. Rev. B* **97**, 045152 (2018).
- [19] Shen, H. & Fu, L. Quantum oscillation from in-gap states and non-Hermitian Landau level problem. *Phys. Rev. Lett.* **121**, 026403 (2018).
- [20] Okawa, M., Ishida, Y., Takahashi, M., Shimada, T., Iga, F., Takabatake, T., Saitoh, T. & Shin, S. Hybridization gap formation in the Kondo insulator YbB₁₂ observed using time-resolved photoemission spectroscopy. *Phys. Rev. B* **92**, 161108(R) (2015).
- [21] Sugiyama, K., Iga, F., Kasaya, M., Kasuya, T. & Date, M. Field-induced metallic state in YbB₁₂ under high magnetic field. *J. Phys. Soc. Jpn.* **57**, 3946-3953 (1988).
- [22] Terashima, T. T., Ikeda, A., Matsuda, Y. H., Kondo, A., Kindo, K. & Iga, F. Magnetization process of the Kondo insulator YbB₁₂ in ultrahigh magnetic fields. *J. Phys. Soc. Jpn.* **86**, 054710 (2017).
- [23] Ohashi, T., Koga, A., Suga, S. & Kawakami, N. Field-induced phase transitions in a Kondo insulator. *Phys. Rev. B*, **70**, 245104 (2004).
- [24] Ghannadzadeh, S., Coak, M., Franke, I., Goddard, P. A., Singleton, J. & Manson, J. L. Measurement of magnetic susceptibility in pulsed magnetic fields using a proximity detector oscillator. *Rev. Sci. Instrum.* 82, 113902 (2011).
- [25] Shoenberg, D. *Magnetic Oscillations in Metals*. (Cambridge University Press, Cambridge, England, 1984).
- [26] These results are consistent with the "back projection" approach [27] for the measured SdH frequency (Supplementary Information). Furthermore, the *H*-dependence of the slope of the nonlinear Landau diagram shown in Fig. 1c scales with the back projection of the *M* curves, suggesting that the evolution of the FS may be reflected in *M* (see Supplementary Information).
- [27] van Ruitenbeek, J. M., Verhoef, W. A., Mattocks, P. G., Dixon, A. E., van Deursen, A. P. J. & de Vroomen, A. R. A de Haas-van Alphen study of the field dependence of the Fermi surface in ZrZn₂, *J. Phys. F: Met. Phys.* **12**, 2919-2928 (1982).
- [28] Götze, K. *et al.* Unusual phase boundary of the magnetic-field-tuned valence transition in CeOs₄Sb₁₂. *Phys. Rev. B* **101**, 075102 (2020).
- [29] Yang, Y-F. & Pines, D. Emergent states in heavy-electron materials. *Proc. Natl. Acad. Sci. USA* **109**, E3060-E3066 (2012).
- [30] Jacko, A. C., Fjærestad, J. O. & Powell, B. J. A unified explanation of the Kadowaki-Woods ratio in strongly correlated metals. *Nat. Phys.* **9**, 422 (2009).

- [31] Hussey, N. E. Non-generality of the Kadowaki-Woods ratio in correlated oxides. *J. Phys. Soc. Jpn* **74**, 1107-1110 (2005).
- [32] Tsujii, N., Kontani, H., & Yoshimura, K. Universality in heavy fermion systems with general degeneracy. *Phys. Rev. Lett.* **94**, 057201 (2005).
- [33] Matsumoto, Y., Kuga, K., Tomita, T., Karaki, Y. & Nakatsuji, S. Anisotropic heavy-Fermi-liquid formation in valence-fluctuating α-YbAlB₄. *Phys. Rev. B* **84**, 125126 (2011).
- [34] Harrison, N. *et al.* Unconventional quantum fluid at high magnetic fields in the marginal chargedensity-wave system. α –(BEDT-TTF)₂MHg(SCN)₄ (M = K and Rb). *Phys. Rev. B* **69**, 165103 (2004).
- [35] Singleton, J., Nicholas, R.J., Nasir, F. & Sarkar, C. K. Quantum transport in accumulation layers on Cd_{0.2}Hg_{0.8}Te. *J. Phys. C: Solid State Phys*, **19** 35 (1986).
- [36] Quader, K. F., Bedell, K. S. & Brown, G. E. Strongly interacting fermions. *Phys. Rev. B* **36**, 156-167 (1987).
- [37] Senthil, T., Sachdev, S. & Vojta, M. Fractionalized Fermi liquids. *Phys. Rev. Lett.* **90**, 216403 (2003).
- [38] Senthil, T., Vojta, M. & Sachdev, S. Weak magnetism and non-fermi liquids near heavy-fermion critical points. *Phys. Rev. B* **69**, 035111 (2004).
- [39] Patel, A. A., McGreevy, J., Arovas, D. P. & Sachdev, S. Magnetotransport in a model of a disordered strange metal. *Phys. Rev. X* **8**, 021049 (2018).
- [40] Leadley, D. R., Nicholas, R. J., Foxon, C. T. & Harris, J. J. Measurements of the effective mass and scattering times of composite fermions from magnetotransport analysis. *Phys. Rev. Lett.* **72**, 1906 (1994).
- [41] Nagaosa, N. Emergent electromagnetism in condensed matter. *Proc. Jpn. Acad.*, *Ser. B* **95**, 278-289 (2019).

Methods

Sample preparation and pulsed field facilities. YbB₁₂ single crystals were grown by the traveling-solvent floating-zone method [42]. The two samples studied in this work were cut from the same ingot and shown to have almost identical physical properties, including the SdH oscillations below the I-M transition, in our previous investigations [1, 3]. The YbB₁₂ sample characterized in the magnetostriction and the magnetization (*M*) measurements corresponds to sample N1 in Ref. [1] and #2 in Ref. [3], whereas the high-field MR was measured in the YbB₁₂ sample N3 in Ref. [1], which is also crystal #1 in Ref. [3]. Both samples were used in the PDO experiments. The PDO data from N3 taken at a fixed field direction were published elsewhere [1]. X-ray diffraction measurements on sample N1 show clear (00*l*) series Bragg peaks (Extended Data Fig. 4) with no indication of crystalline impurity phases.

Magnetostriction and M of YbB₁₂ samples were measured in a capacitor-driven 65 T pulsed magnet at NHMFL, Los Alamos. In the PDO and MR measurements, fields were provided by 65 T pulsed magnets and a 75 T Duplex magnet. Temperatures down to 500 mK were obtained using a 3 He immersion cryostat. A 4 He cryostat was also used for MR measurements above 1.4 K.

Magnetostriction measurements. The linear magnetostriction $\Delta L/L$ of YbB₁₂ was measured using a fibre Bragg grating dilatometry technique [43, 44]. In our setup (Extended Data Fig. 1), the dilatometer is a 2 mm-long Bragg grating contained in a 125 μ m telecom-type optical fibre. The oriented YbB₁₂ single crystal was attached to the section of fibre with the Bragg grating using a cyanoacrylate adhesive. The crystallographic [100] direction was aligned with the fibre, which is also parallel to H. Thus, we measure the longitudinal magnetostriction along the a-axis of cubic YbB₁₂. The magnetostriction $\Delta L/L$ was extracted from the shift of the Bragg wavelength in the reflection spectrum [44]. The signal from an identical Bragg grating on the same fibre with no sample attached was subtracted as the background.

In a paramagnetic metal, the high-field longitudinal magnetostriction contains both M^2 and M^3 terms [45]. In this sense, the power-law H dependence of $\Delta L/L$ with an exponent ≈ 3.5 (Extended Data Fig. 1b) is consistent with the weak superlinear M in YbB₁₂ at 40 K [21]. As T lowers, $\Delta L/L$ decreases and a nonmonotonic field dependence develops at 30 K (Extended Data Fig. 1b). We note that the fast suppression of $\Delta L/L$ coincides with the sharpening of the I-M transition in the derived susceptibility below 30 K [46], suggesting an additional energy scale in YbB₁₂ that is much lower than the Kondo temperature $T_{\rm K} \approx 240$ K and the gap opening temperature $T_{\rm g} \approx 110$ K

[20]. Below 5 K, $\Delta L/L$ becomes quite small and a step-like feature is observed with an onset at $\mu_0 H = 46.3$ T, perfectly aligned with the sudden increase in M (Extended Data Fig. 1c,d). We identify this characteristic field as the I-M transition field $H_{\text{I-M}}$ at which a metamagnetic transition also happens [2, 22, 46]. A negative volume magnetostriction is characteristic of mixed-valence Yb compounds in which the volume of nonmagnetic Yb²⁺ (4 f^{14}) is 4.6% smaller than that of magnetic Yb³⁺ (4 f^{13}). Therefore a volume decrease with increasing H is expected [47, 48]. The step-like decrease at $H_{\text{I-M}}$ (Extended Data Fig. 1c) may therefore be evidence that the sudden shrinkage results from a valence transition of the Yb ions. Using a simple isotropic assumption, the change of volume magnetostriction at $H_{\text{I-M}}$ is $\delta(\Delta V/V) = 3\delta(\Delta L/L) \simeq 6 \times 10^{-6}$, corresponding to a valence increase of 0.00013. Such a small average valence enhancement implies a quite weak and incomplete breakdown of the Kondo screening. Consequently, the state immediately above $H_{\text{I-M}}$ is confirmed to be a KM in which mixed-valence features persist.

Magnetization measurements. M was measured using a compensated-coil susceptometer [49, 50]. The 1.5 mm bore, 1.5 mm long, 1500-turn coil was made of 50 gauge high-purity copper wire. The sample was inserted into a 1.3 mm diameter non-magnetic ampoule that can be moved in and out of the coil. When pulsed fields are applied, the coil picks up a voltage signal $V \propto (dM/dt)$, where t is the time. Numerical integration is used to obtain M and a signal from the empty coil measured under identical conditions is subtracted. Pulsed-field M data are calibrated using the M of a YbB₁₂ sample of known mass measured in a Quantum Design VSM magnetometer [3].

As shown in Extended Data Fig. 1d, a metamagnetic transition occurs at 46.3 T, coinciding with the onset of the step-like feature in the magnetostriction. This observation further confirms the location of $H_{\text{I-M}}$ in our YbB₁₂ samples. At the highest H used in this experiment, $M \approx 1 \mu_{\text{B}}/\text{Yb}$, so that M contributes only $\sim 0.2\%$ of B. Therefore we can ignore the M term and equate B to the external magnetic field, *i.e.*, $B \approx \mu_0 H$.

Radio frequency measurements of resistivity using the PDO technique. The PDO circuit [24, 51] permits convenient contactless measurements of the resistivity of metallic samples in pulsed magnetic fields. In our experiments, a 6-8 turn coil made from 46 gauge high-purity copper wire is tightly wrapped around the YbB₁₂ single crystals and secured using GE varnish. The coil is connected to the PDO, forming a driven LC tank circuit with a resonant frequency of 22-30 MHz at cryogenic T and H = 0. The output signal is fed to a two-stage mixer/filter heterodyne detection system [24], with mixer IFs provided by a dual-channel BK-Precision Function/Arbitrary

Waveform Generator. The second mixer IF was 8 MHz, whereas the first mixer IF was adjusted to bring the final frequency down to \approx 2 MHz. The resulting signal was digitized using a National Instruments PXI-5105 digitizer.

Considering all the contributions, the shift in PDO frequency f due to H is written as [1, 24]

$$\Delta f = -a\Delta L - b\Delta R,\tag{4}$$

where a and b are positive constants determined by the frequency plus the capacitances, resistances and inductances in the circuit, L is the coil inductance and R is the resistance of the coil wire and cables. In the case of a metallic sample, the coil inductance L depends on the skin depth λ of the sample. If we assume that the sample magnetic permeability μ and the coil length stay unchanged during a field pulse, we have $\Delta L \propto (r - \lambda)\Delta \lambda$, where r is the sample radius. At angular frequency ω , the skin depth is proportional to square root of the resistivity ρ :

$$\lambda = \sqrt{\frac{2\rho}{\omega\mu}}. (5)$$

Therefore, for a metallic sample, the resonance shift Δf reflects the sample MR and the detected quantum oscillations are due to the SdH effect. In YbB₁₂, the PDO measurement only detects the signal from the sample in the high-field KM state, *i.e.*, when $H > H_{\text{I-M}}$ [1]. In the low-field KI state the sample is so resistive that the skin depth λ is larger than the sample radius r. As a result, Δf mainly comes from the MR of the copper coil [24]. The "dip" in PDO f in Fig. 1a consequently indicates where the skin depth is comparable to the sample radius and provides an alternative means to find $H_{\text{I-M}}$. We note that the $H_{\text{I-M}}$ assigned to onset of the "dip" feature (see Extended Data Table 1) is ≈ 0.2 T lower than the metamagnetic transition in Extended Data Fig. 1.

Onsager relationship for a field-dependent Fermi surface. The Onsager relation [25] relates the frequency F of quantum oscillations to the FS extremal orbit area A: $F = \frac{\hbar}{2\pi e}A$. Textbook derivations [25] invoke the Correspondence Principle to give an orbit-area quantization condition $(N+\lambda)\frac{2\pi eB}{\hbar}=A$, where N is a quantum number and λ is a phase factor. The derivation makes no assumptions about A being constant, so for a field-dependent A=A(B), we can write

$$(N+\lambda)\frac{2\pi eB_N}{\hbar} = A(B_N), \tag{6}$$

where B_N is the magnetic induction at which the N^{th} oscillation feature (peak, valley, etc.) occurs. Evaluating Eq. 6 for N and N+1 and taking the difference gives

$$\frac{A(B_{N+1})}{B_{N+1}} - \frac{A(B_N)}{B_N} = \frac{2\pi e}{\hbar}.$$
 (7)

From an experimental standpoint, in materials where F is constant, a particular feature of a quantum oscillation is observed whenever $N + \lambda' = \frac{F}{B}$; λ' is another phase factor. Allowing F to vary (i.e., F = F(B)), evaluating the expression for N and N + 1 and taking the difference yields

$$\frac{F(B_{N+1})}{B_{N+1}} - \frac{F(B_N)}{B_N} = 1. {8}$$

A comparison of Eqs. 7 and 8 shows that the Onsager relation still holds, i.e., $F(B) = \frac{\hbar}{2\pi e} A(B)$.

In Fig. 2a, $B^* = \mu_0 H^* = 41.6 \,\mathrm{T}$ is subtracted from the applied field to yield linear Landau-index diagrams for $\theta \leq 20.7^{\circ}$. The resulting fit is described by $N + \lambda = \frac{F_0}{(B_N - B^*)}$ (Eq. 2), which can be written in terms of a *B*-dependent frequency $N + \lambda = \frac{F(B_N)}{B_N}$, where $F(B) = \frac{F_0 B}{(B - B^*)}$ (Eq. 3). Following the reasoning given above, this is associated with a *B*-dependent extremal area

$$A(B) = \frac{A_0}{B - B^*} B$$
, with $A_0 = \frac{2\pi e}{\hbar} F_0$. (9)

In the Supplementary Information, we show that the analysis presented here is functionally equivalent to the "back-projection" method [26]. Note that we have not considered the Zeeman splitting of the peaks, so that Eqs. 3 and 9 describe the average of the spin-up and spin-down components.

Spin-splitting parameter. The spin-splitting parameter S is introduced to describe the Zeeman splitting of the quantum oscillation peaks/valleys. In the most straightforward scenario, the magnetic inductions $B_N^{+(-)}$ at which the spin-down(up) component of the N^{th} Landau tube reaches the Fermi surface are given by:

$$\frac{F}{B_N^{\pm}} = N + \lambda \pm \frac{1}{2}S. \tag{10}$$

Therefore, S causes a term in addition to the phase factor λ , which has opposite signs for the spin-down and spin-up Landau sheets. According to Eq. 10, the value of S can be obtained from multiplying the interval of the spin-split peak/valleys (in 1/B) by the oscillation frequency F. In Fig. 2d, S for nonlinear (Fig. 1c) and linear (Fig. 2a) Landau level plots are calculated as $S = F_{\rm m}(1/B_N^+ - 1/B_N^-)$ and $S = F_0[1/(B_N^+ - B^*) - 1/(B_N^- - B^*)]$, respectively. Here $F_{\rm m}$ represents the oscillation frequency extracted directly from the slope of the nonlinear Landau level plot (see Supplementary Information and Extended Data Fig. 6b). We mention that these two approaches yield the same values of S (Fig. 2d, $\theta = 10.9^\circ$ data).

As pointed out by Shoenberg [25], the effect of Zeeman splitting on oscillation extrema is determined by the cyclotron mass m^* and g-factor:

$$S = \frac{1}{2}g\frac{m^*}{m_0},\tag{11}$$

which provides a simple method to evaluate the *g*-factor in the system. As shown in Fig. 2d, with a *g*-factor of 0.084, the field dependence of *S* can be mapped adequately onto the mass enhancement. Such behaviour does not only prove the validity of our Zeeman splitting analysis of the SdH effect, but also reveals an unusually small *g*-factor that may reflect the exotic nature of the corresponding quasiparticle band.

Resistivity measurements in the KM state. From $\mu_0H=0$ to 60 T, the resistivity of YbB₁₂ decreases by five orders of magnitude [1]. As a result, MR measurements in pulsed fields are challenging. If a constant current is used during the entire field pulse, either the signal-to-noise ratio is poor in the KM state, or the high resistance in the KI state causes serious Joule heating. To solve this issue, we developed a pulsed-current technique. The experimental setup is shown in Extended Data Fig. 3a. A ZFSWHA-1-20 isolation switch is used to apply current pulses with widths < 10 ms. The switch is controlled by two square wave pulses generated by a BK-Precision Model 4065 dual-channel function/arbitrary waveform generator triggered by the magnet pulse. Thus, a relatively large electric current (2-3 mA) can pass through the sample during a narrow time window within the field pulse (Fig. 3a, inset).

Current is applied only when YbB₁₂ enters the KM state. In our low-*T* MR measurements, the switch turns on at 47 T during the upsweeps and turns off at 47 T during the downsweeps. To reduce heating due to eddy currents, we measured the longitudinal MR of a needle-shaped sample (length 6.5 mm between voltage leads; cross-sectional area 0.33 mm²). As shown in Extended Data Fig. 3b, the downsweeps still suffer some Joule heating. Hence, in the main text we focus on the upsweeps, which show very weak longitudinal MR and should reflect the intrinsic electrical transport properties of the KM state of YbB₁₂. (During the experiments we found that when we attempted to stabilize the target temperature by applying a high heater excitation in an environment of dense ³He vapour, the temperature reading according to the thermometer could be lower than the actual sample temperature. We removed all the data points measured using this procedure.)

According to Eq. 9, A(B) for the pocket detected in the PDO measurement shrinks by $\simeq 45\%$ from 50 T to 60 T. Assuming a spherical FS, this corresponds to an $\simeq 60\%$ reduction in quasiparticle density n. Meanwhile, the cyclotron mass increases by $\simeq 60\%$ (Fig. 2b, inset). Consequently, a textbook Drude expression $\rho = m^*/ne^2\tau$ (τ is the relaxation time) predicts that the resistivity would increase by a factor ≈ 4 from 50 T to 60 T if the electrical transport is dominated by this pocket. In sharp contrast, almost no MR is observed in this field range (Extended Data Fig. 3),

indicating the negligible contribution of this FS pocket to the electrical transport.

On the other hand, the weak MR and the *T*-linear resistivity of the KM state between 4 K and 9 K are in agreement with the predicted behaviour of a marginal Fermi liquid (without macroscopic disorder) or an incoherent metal, potential evidence for the coexistence of fermions inactive in the charge transport and more conventional charged fermions [39].

The Kadowaki-Woods ratio. For the Sommerfeld coefficient γ in the KM state of YbB₁₂, a pulsed-field heat capacity study reports values of 58 mJ mol⁻¹ K⁻² and 67 mJ mol⁻¹ K⁻² at 49 T and 60 T, respectively [2]. A linear interpolation gives $\gamma = 63$ mJ mol⁻¹ K⁻² at 55 T. Since $\gamma = (\pi^2 k_{\rm B}^2/3)N(E_{\rm F})$ and the density of states at the Fermi energy $N(E_{\rm F}) = (m^*/\pi^2\hbar^2)(3\pi^2n)^{1/3}$, the Sommerfeld coefficient can be written as:

$$\gamma = \frac{\pi^2 k_B^2}{3} \frac{m^* k_F}{\pi^2 \hbar^2},\tag{12}$$

where $k_{\rm F}$ is the Fermi vector. As for the FS pocket detected in the SdH measurement, Eq. 3 gives $F(55\,{\rm T})=231.9\,{\rm T}$. In a spherical FS model, $F=\hbar k_F^2/2e$, $n=k_F^3/3\pi^2=(2eF/\hbar)^{3/2}/3\pi^2$ ($k_{\rm F}$ is the Fermi wavevector), therefore $F=231.9\,{\rm T}$ corresponds to $n=1.99\times10^{19}\,{\rm cm}^{-3}$. Also, for 55 T, $m^*\simeq10\,{\rm m}_0$, based on Fig. 2b (inset). Putting these parameters into Eq. 12, we estimate that the FS pocket responsible for the SdH effect could contribute only 4.4% of the measured γ . Consequently, an additional band with a much larger density of states must exist in the KM state of YbB₁₂.

The unusually large KW ratio (Fig. 3c) suggests the somewhat unusual nature of the heavy quasiparticles that dominate the charge transport and thermal properties of the KM state. Analysis of the KW ratio shows that for a single-band, strongly correlated system, the value of A_2/γ^2 does not depend on the strength of correlations but is instead solely determined by the underlying band structure [30]. We consider the simplest case of a single-band isotropic Fermi-liquid model. Using the same calculations as in Ref. [30], we have:

$$A_2 = \frac{81\pi^3 k_B^2 (m^*)^2}{4e^2\hbar^3 k_E^5}.$$
 (13)

Taken together, Eqs. 12 and 13 yield $k_{\rm F} = 2.15~{\rm nm}^{-1}$ (corresponding to $n = 3.36 \times 10^{20}~{\rm cm}^{-3}$) and a rather large effective mass of $m^* = 90.0~{\rm m}_0$. Such a heavy mass is unusual for Yb-based mixed-valence compounds, but explains the anomalous KW ratio as well as the absence of SdH oscillations due to these quasiparticles in the PDO response.

SdH oscillations due to charge-neutral quasiparticles. Magnetic quantum oscillations are observed in both M and ρ in the KI state of YbB₁₂ with their behaviours follow the description of

the LK formula [1]. The size of the FS and the effective mass of the quasiparticles inferred from the oscillations are consistent with the fermion-like contribution to the thermal conductivity [3]. A natural explanation, given the high electrical resistivity, is that the thermal conductivity and quantum oscillations are due to charge-neutral fermions.

Of the two oscillatory effects observed in the KI state, the dHvA effect is the more fundamental. As pointed out by Lifshitz, Landau and others [25], it involves oscillations in a thermodynamic function of state (M) that may be related to the electronic density of states with a minimum of assumptions. The fact that M in the KI state oscillates as a function of H can only be due to the oscillation of the fermion density of states, and consequently their free energy.

Even in conventional metals, quantum oscillations in ρ are harder to model quantitatively. A starting point was suggested by Pippard [52]; the rate at which quasiparticles scatter will depend on the density of states available via *Fermi's Golden Rule*. Hence, if the quasiparticle density of states oscillates as a function of H, the scattering rate τ^{-1} and consequently ρ will also oscillate proportionally, leading to the SdH effect.

Before modifying this idea to tackle the SdH effect in the KI state, we remark that the *H*-dependent frequency of the oscillations in the KM state suggests that exchange of fermions between charge-neutral and conventional FS sections occurs readily, probably via low-energy scattering. This is also supported by the *T*-linear resistivity [39] (Fig. 3a). The rate at which this scattering happens will obviously reflect the joint density of fermion states.

Returning to the KI state of YbB₁₂, ρ is thought to be due to charge carriers thermally excited across the energy gap, plus contributions from states in the gap that lead to the ρ saturation at low T. Following the precedent of the KM state, it is likely that fermions in the KI state scatter back and forth between the charge-neutral states and the more conventional bands. The situation is more complicated than Pippard's original concept because scattering *between* two bands is involved. Nevertheless, the amount of scattering will be determined by the joint density of states, and, because the density of states of the neutral quasiparticles oscillates with H, so will ρ [53]. Unlike conventional metals, the density of the charge carriers will be T-dependent, so the amplitude of the SdH oscillations in the KI state will follow a different T-dependence from that of the dHvA oscillations, as observed in experiments [1].

As described by Eq. 4, the PDO f in the KM state is determined by the skin depth, *i.e.*, the conductivity. As described above, scattering of fermions occurs between the charge-neutral states and more conventional bands; in the KM state, our conductivity results and the heat capacity data

of others suggests that the latter is a FS of heavy charged fermions. The SdH effect in conductivity caused by the oscillatory density of states of the neutral quasiparticles in magnetic fields is detected in the PDO experiments. By contrast, any intrinsic quantum oscillations due to the metallic FS will be suppressed by a combination of the very heavy effective mass and the relatively high $T (\geq 0.5 \text{ K})$ of our measurements.

[42] Iga, F., Shimizu, N. & Takabatake, T. Single crystal growth and physical properties of Kondo insulator YbB₁₂. *J. Magn. Magn. Mater.* **177-181**, 337-338 (1998).

- [43] Daou, R., Weickert, F., Nicklas, M., Steglich, F., Haase, A. & Doerr, M. High resolution magnetostriction measurements in pulsed magnetic fields using fibre Bragg gratings. *Rev. Sci. Instrum.* **81**, 033909 (2010).
- [44] Jaime, M. *et al.* Fiber Bragg Grating Dilatometry in Extreme Magnetic Field and Cryogenic Conditions. *Sensors.* **17**, 2572 (2017).
- [45] Mushnikov, N. V. & Goto, T. High-field magnetostriction of the valence-fluctuating compound YbInCu₄. *Phys. Rev. B* **70**, 054411 (2004).
- [46] Matsuda, Y. H., Kakita, Y. & Iga, F. The temperature dependence of the magnetization process of the Kondo insulator YbB₁₂. *Crystals* **10**, 26 (2020).
- [47] Yoshimura, K., Nitta, T., Mekata, M., Shimizu, T., Sakakibara, T., Goto, T. & Kido, G. Anomalous high-field magnetization and negative forced volume magnetostriction in $Yb_{1-x}M_xCu_2$ (M = In and Ag) evidence for valence change in high magnetic fields. *Phys. Rev. Lett.* **60**, 851 (1988).
- [48] Zieglowski, J., Häfner, H. U. & Wohlleben, D. Volume magnetostriction of rare-earth metals with unstable 4f shells. *Phys. Rev. Lett.* **56**, 193 (1986).
- [49] Goddard, P. A., Singleton, J., Lima Sharma, A. L., Morosan, E., Blundell, S. J., Bud'ko, S. L. & Canfield, P. C. Separation of energy scales in the kagome antiferromagnet TmAgGe: A magnetic-fieldorientation study up to 55 T. *Phys. Rev. B* **75**, 094426 (2007).
- [50] Goddard, P. A. *et al.* Experimentally determining the exchange parameters of quasi-two-dimensional Heisenberg magnets. *New J. Phys* **10**, 083025 (2008).
- [51] Altarawneh, M. M., Mielke, C. H. & Brooks, J. S. Proximity detector circuits: An alternative to

- tunnel diode oscillators for contactless measurements in pulsed magnetic field environments. *Rev. Sci. Instrum.* **80**, 066104 (2009).
- [52] Pippard, A. B. The Dynamics of Conduction Electrons. (Blackie & Son, Glasgow, 1965).
- [53] We also mention that a hypothetical model of the SdH effect in a system containing gapless neutral fermions and gapped charged bosons has been established by Sodemann *et al*, which predicts LK behaviour above a certain *T* [18].

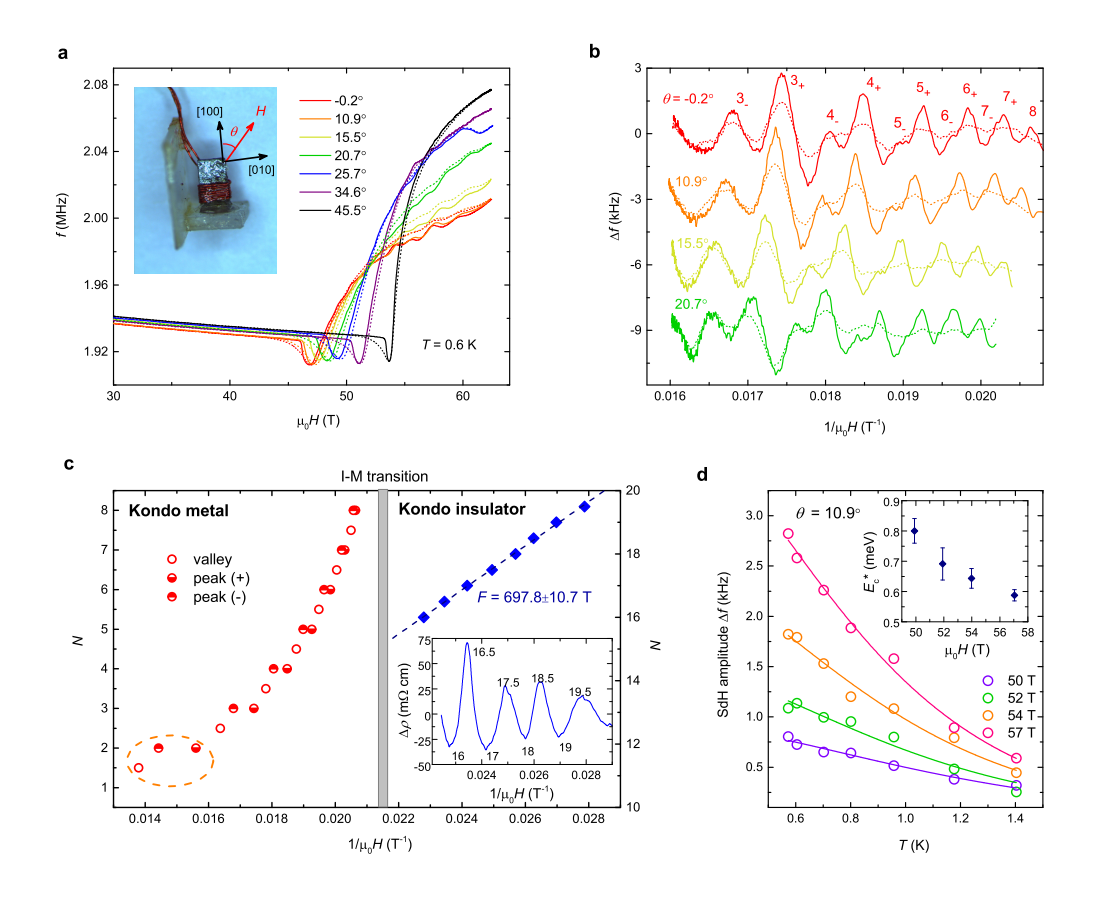


Fig. 1. The SdH effect in YbB₁₂. a, The PDO frequency f for a YbB₁₂ single-crystal sample, measured at $T = 0.6 \,\mathrm{K}$ at various tilt angles θ up to 62.5 T. The "dip" feature in f corresponds to the I-M transition which shifts to higher field at larger tilt angles. Solid lines and short-dashed lines are upsweeps and downsweeps, respectively. Inset: a photograph of the device we used in pulsed-field PDO experiments. The whole device was attached to a rotation stage with the rotation axis normal to the (001)-plane. The tilt angle θ is defined as the angle between the field vector **H** and the crystallographic [100] direction. **b**, Oscillatory component of the PDO frequency, Δf , obtained after a 4th-order polynomial background subtraction from the raw data shown in a for different tilt angles from $\theta = 0.2^{\circ}$ to $\theta = 20.7^{\circ}$. The numbers beside the SdH peaks are the Landau level indices. The signs "+" and "-" mark the spin-split Landau sublevels with inferred Zeeman shift $+g\mu_B B/2$ (spin-down) and $-g\mu_B B/2$ (spin-up), respectively. The SdH effect is weaker on the downsweeps (short-dashed lines), probably due to sample heating. c, Landau-level plots for YbB_{12} in the low-field KIstate (blue diamonds) and the high-field KM state (red circles), both under a magnetic field along the [100] direction. Data points in the orange dashed circle were taken in the 75 T Duplex magnet (Extended Data Fig. 2). The gray vertical bar denotes the I-M transition. The inset shows the SdH oscillations in the KI state of YbB₁₂. **d,** T dependence of Δf at different fields. Data was taken at $\theta = 10.9^{\circ}$ (Extended Data Fig. 2b). Solid lines are the Lifshitz-Kosevich (LK) fits. Inset: the field dependence of the fitted cyclotron energy E_c^* .

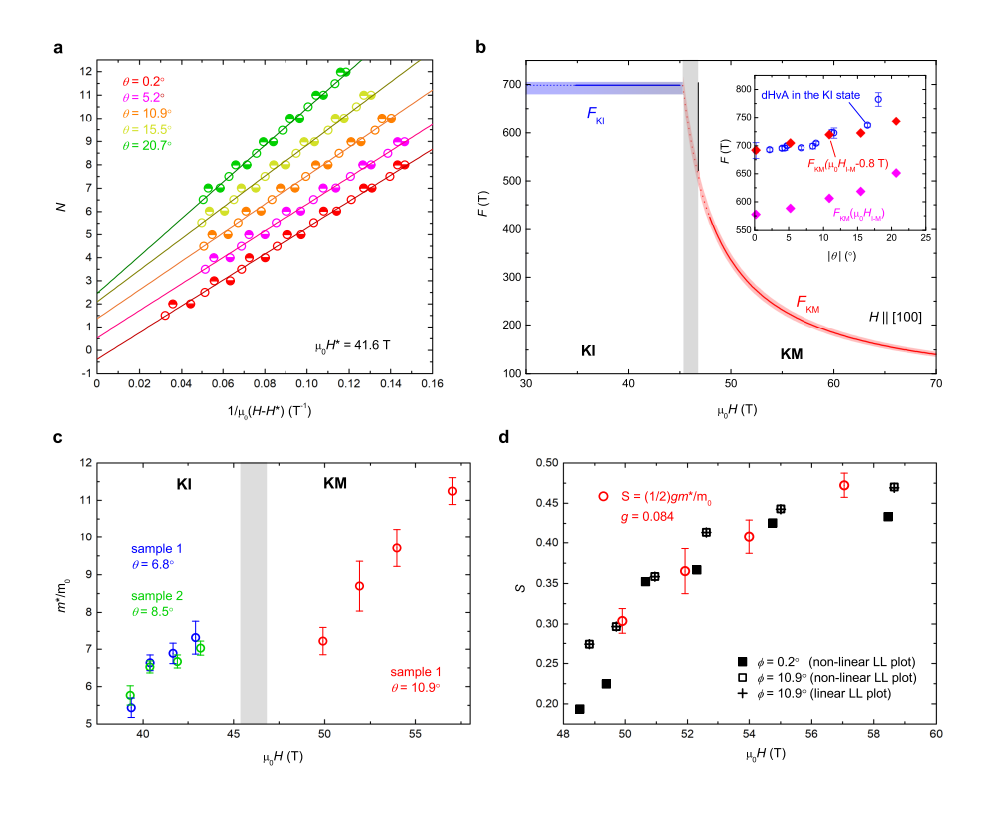


Fig. 2. The field-dependent Fermi surface in the metallic state. a, The nonlinear Landau level plots shown in Fig. 1c become linear after adding an offset of $\mu_0 H^* = 41.6 \,\mathrm{T}$ to the applied magnetic field. The linear fits yield slopes (Extended Data Table 1) which are denoted by the parameter F_0 in Eq. 3. The Landau diagrams are shifted vertically by index N = 1 for clarity. **b**, With field applied along the [100] direction, the quantum oscillations in the KI state exhibits a field-independent frequency F_{KI} (Fig. 1c), whereas in the KM state the SdH frequency $F_{\rm KM}$ is described by Eq. 3. Solid lines and short-dashed lines represent the field range in which SdH oscillations are detected and absent, respectively. The width of the coloured regions denotes the frequency uncertainty, given by the fast-Fourier transform (FFT) peak width (considering both the SdH and the dHvA oscillations) [1] for F_{KI} and the fitting errors in **a** for F_{KM} . The light gray vertical bar marks the I-M transition. A black vertical line represents the maximum allowed mismatch between $F_{\rm KI}$ and $F_{\rm KM}$ of ~ 180 T. Inset: The angle dependence of quantum oscillation frequencies in YbB₁₂. Blue circles are dHvA frequencies in the KI state [1]. Magenta and red diamonds are F_{KM} calculated using Eq. 3 at the transition field $\mu_0 H_{\text{I-M}}$ (Extended Data Table 1) and $B = \mu_0 H_{\text{I-M}}$ -0.8 T, respectively. **c,** The cyclotron mass ratio m^*/m_0 , where m_0 is the free electron mass. Data for the KI state are obtained from the LK fits of the dHvA oscillation amplitudes [1], whereas those for the KM state are inferred from the cyclotron energy E_c^* shown in Fig. 1d. **d**, The spin-splitting parameter S for each SdH peak. S values calculated for the nonlinear (Fig. 1c) and linear (panel a) Landau level plots (see Methods) are denoted by squares and "+" symbols, respectively. The field dependence of S can be scaled to that of the cyclotron mass ratio by 23 choosing g = 0.084 (red circles).

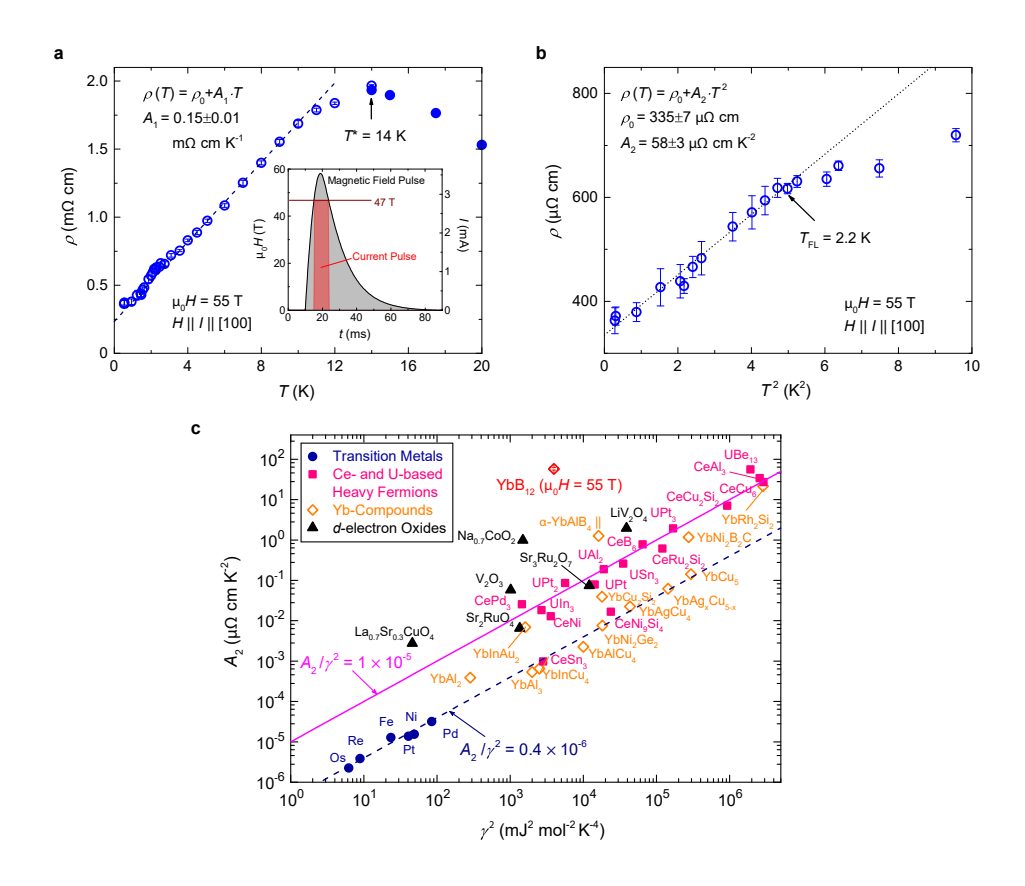
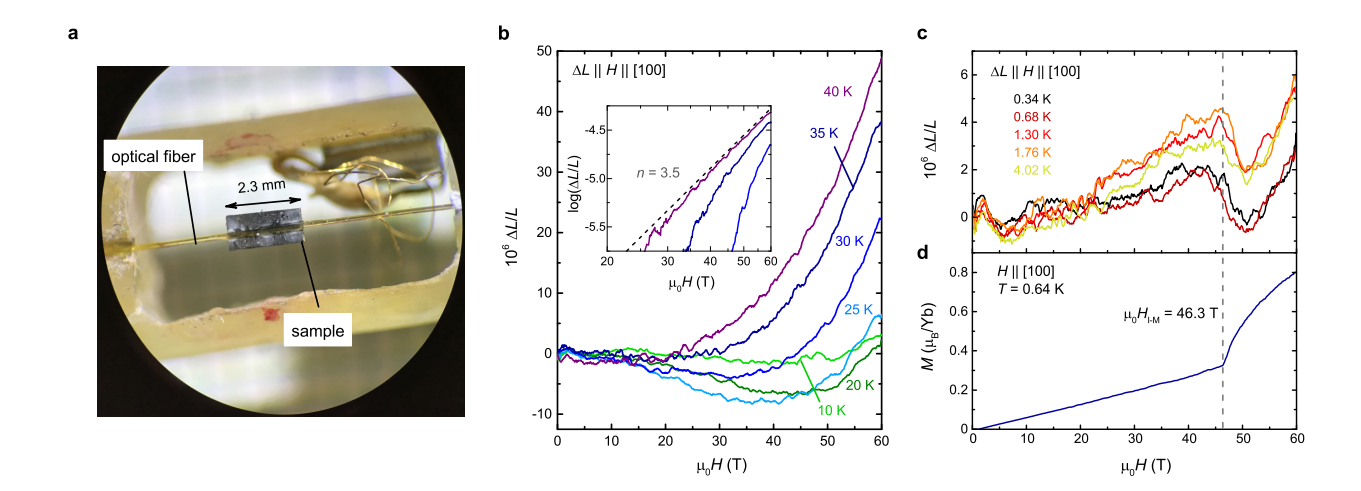
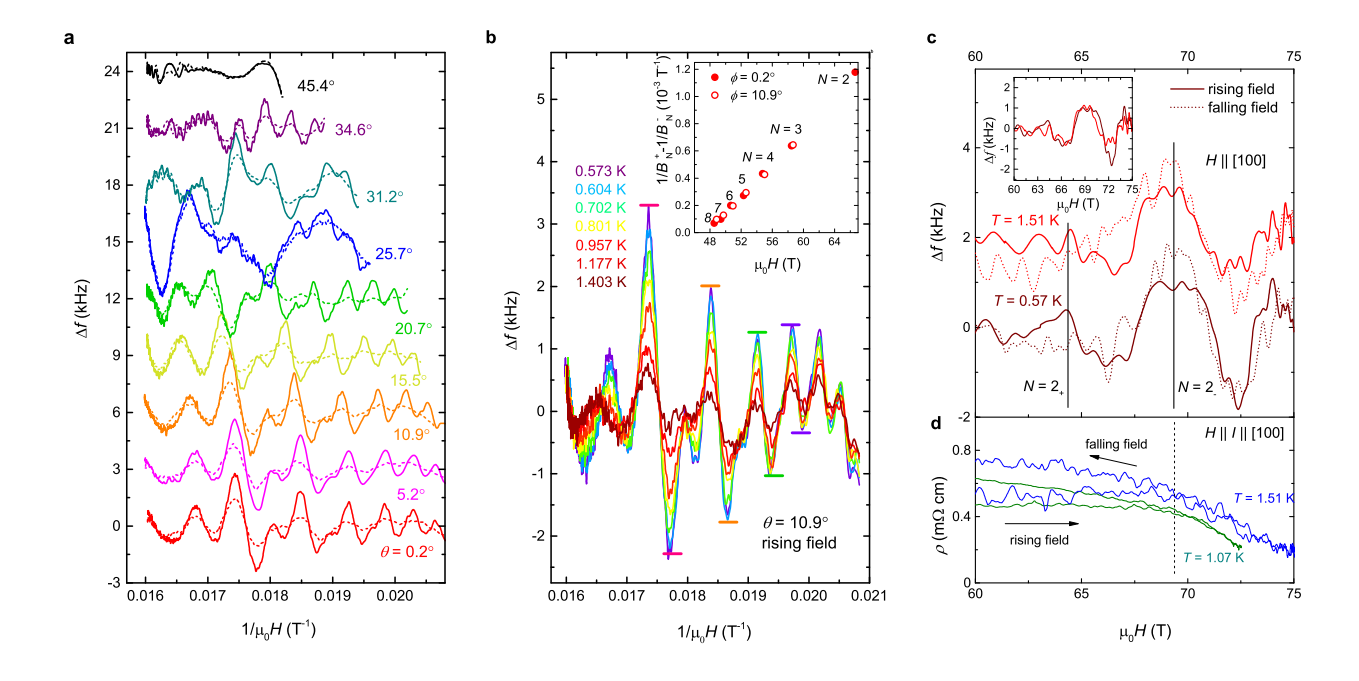


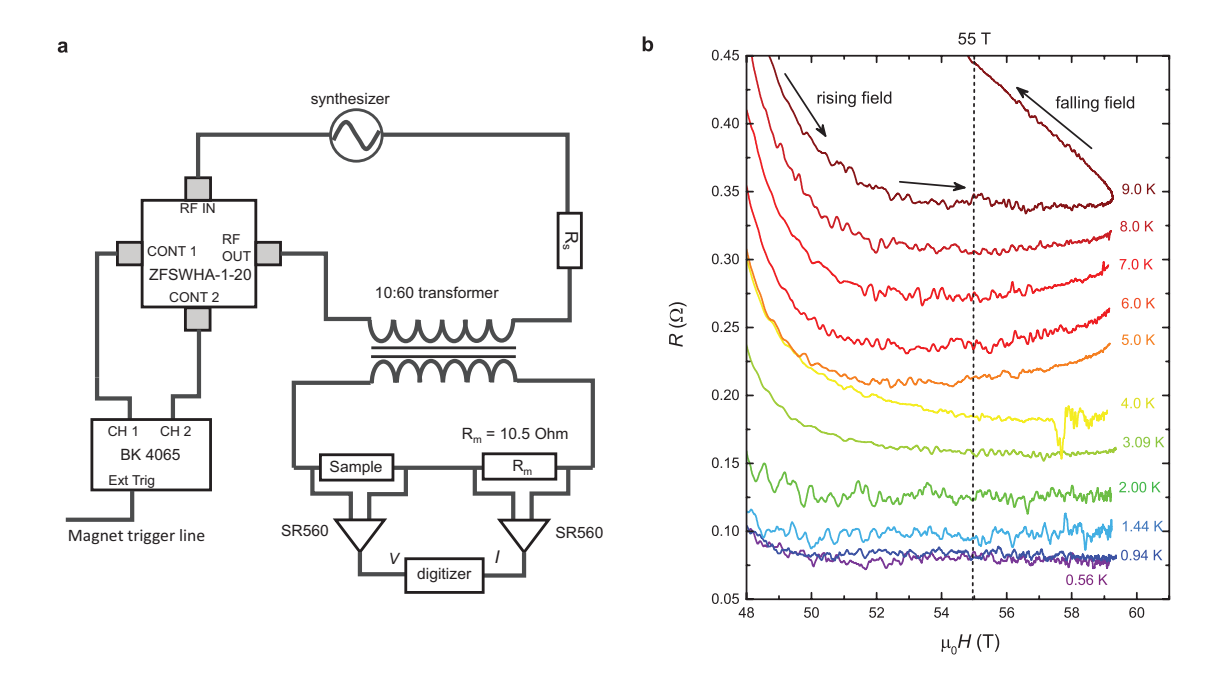
Fig. 3. The temperature dependence of the resistivity in the metallic state. a, The resistivity of YbB₁₂ sample at $\mu_0 H = 55$ T plotted as a function of T. Both the current and the magnetic field were applied along the [100] direction. The hollow symbols are data measured using the pulsed current technique (see Methods). The solid symbols are data taken with a constant excitation in a 3 He gas environment. A maximum in ρ appears at $T^* = 14$ K. The dashed line is a linear fit of $\rho(T)$ from 4 K to 9 K. The inset illustrates the magnetic field pulse and current pulse in our measurement in the time domain. b, The same data plotted against T^2 . The dotted line is a linear fit to the 4 He-liquid data, showing the behaviour of the T^2 -dependence below $T_{\rm FL} = 2.2$ K. c, The deviation of YbB₁₂ from the Kadowaki-Woods relation. We use the value of the Sommerfeld coefficient γ reported for YbB₁₂ in ref. [2]. The data points for transition metals, d-electron oxides and Ce- and U-based heavy fermions are taken from refs. [30, 31], whereas the data for Yb-based compounds are taken from refs. [32, 33].



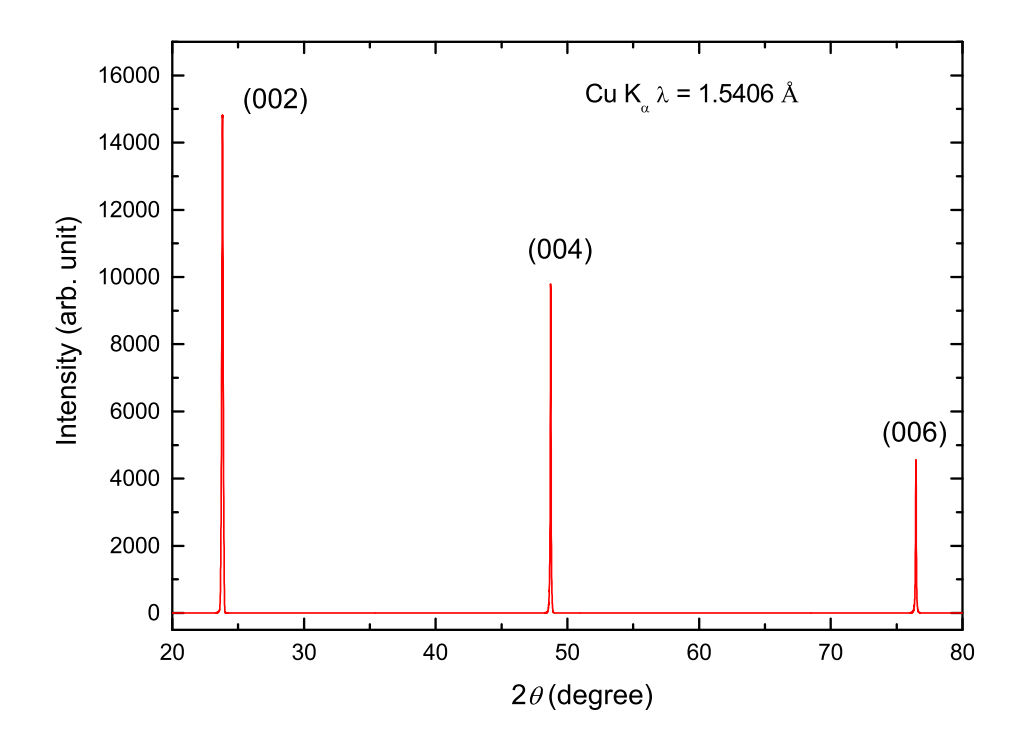
Extended Data Fig. 1. The magnetostriction and magnetization of YbB₁₂. a, The experimental arrangements for magnetostriction measurements. An optical fibre containing fibre Bragg gratings serves as the strain gauge. The single-crystal sample of YbB₁₂ with dimensions $2.3 \times 1.0 \times 0.2$ mm³ is glued to the fibre Bragg grating section of the fibre. A 60 T pulsed magnetic field is applied along the direction of the optical fibre. The longest edge of the single crystal is parallel to the crystallographic a axis, therefore in this arrangement the parallel strain $\Delta L \parallel H \parallel [100]$ is measured. b, Field dependence of the linear magnetostriction $\Delta L/L$ along the a axis at different temperatures ranging from 10 K to 40 K. The inset shows the high-temperature magnetostriction curves in a logarithmic scale. The dashed line is a power-law field dependence with an exponent n = 3.5. c, The linear magnetostriction measured at temperatures below 5 K. d, Magnetization of the same YbB₁₂ single crystal measured at T = 0.64 K using a compensated-coil susceptometer (see Methods). Field was applied along the [100] direction. The gray dashed line indicates the consistency of the step-like decrease in the linear magnetostriction in c and the abrupt increase of magnetization in d at the field-induced I-M transition, $\mu_0 H_{I-M} = 46.3$ T.



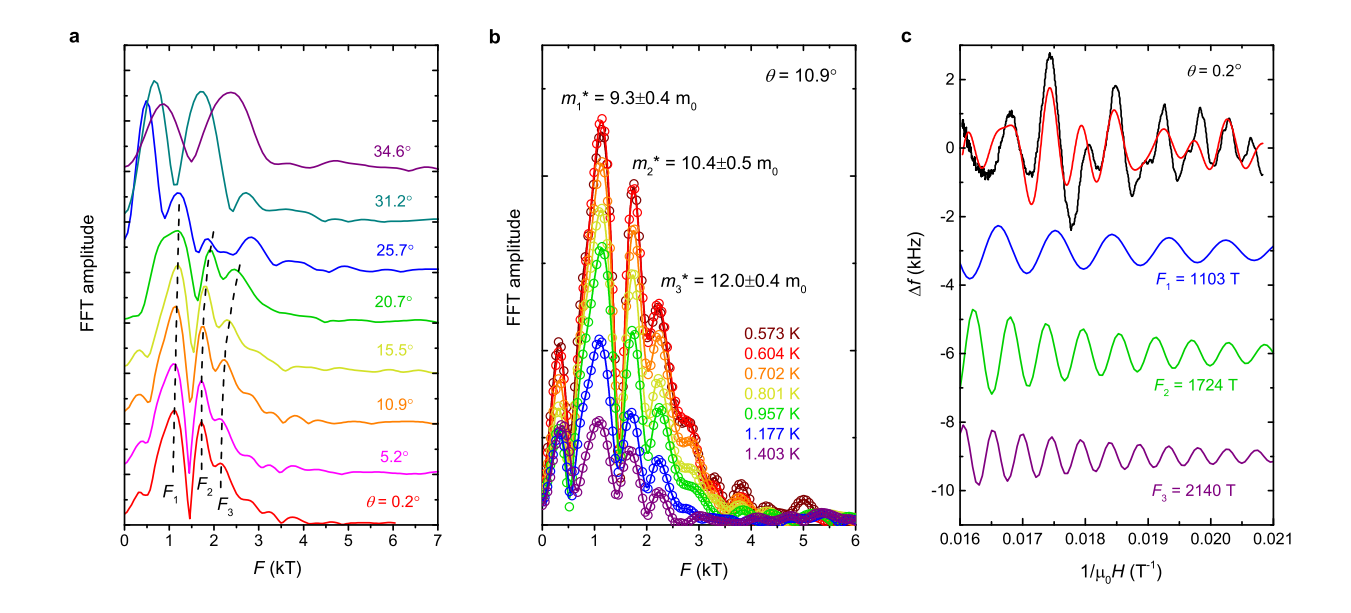
Extended Data Fig. 2. The angle, temperature and field dependence of the SdH effect. a, Oscillatory component of the PDO frequency, Δf , obtained after a 4th-order polynomial background subtraction from raw data at different tilt angles. The SdH effect is weaker in the field downsweeps (short-dashed lines) than in the upsweeps (solid lines), probably due to sample heating. b, Δf taken at $\theta=10.9^{\circ}$ at different temperatures. The field-dependent cyclotron energies shown in Fig. 1d are obtained by fitting the frequency difference between adjacent peaks and valleys to the LK formula. Horizontal bars denote the peaks and valleys used for the fits in Fig. 1d. The inset displays the interval between spin-up and spin-down SdH peaks in inverse magnetic field, as a function of $\mu_0 H$. If the effective mass and the g-factor are field-independent, this value is expected be a constant (see Methods). c, PDO frequency measured up to 75 T in the Duplex Magnet; only the lowest pair of Landau levels, i.e., $N=2_{\pm}$, are shown. The inset shows the small amplitude differences of $N=2_{\pm}$ levels between T=0.57 K and 1.51 K, suggesting a nondiverging quasiparticle mass up to at least 72 T. d, MR measured by the pulsed current technique (see Methods) in the Duplex magnet. A downward kink is observed at 68 T and coincides with the $N=2_{-}$ sublevel. This slope change may imply a crossover to an unknown high-field state in YbB₁₂.



Extended Data Fig. 3. The pulsed current technique. **a,** A schematic diagram of the pulsed current technique used for measuring the MR of YbB₁₂ samples in the KM state (see Methods). The current pulse is triggered with a precisely controlled time delay after the start of the magnetic field pulse. In the measurements we adjust the value of R_s to maintain the excitation amplitude 2-3 mA at different temperatures. **b,** The longitudinal MR of YbB₁₂ in the KM state below 10 K, measured with both field and current applied along the crystallographic [100] direction. The data taken at 1.44 K, 2.00 K and 3.09 K are measured with the sample in 4 He liquid, whereas other curves are measured in 3 He liquid or vapour. The vertical dashed line marks the 55 T field at which we extract resistivity values from the upsweeps for the temperature dependence analysis (see Methods).

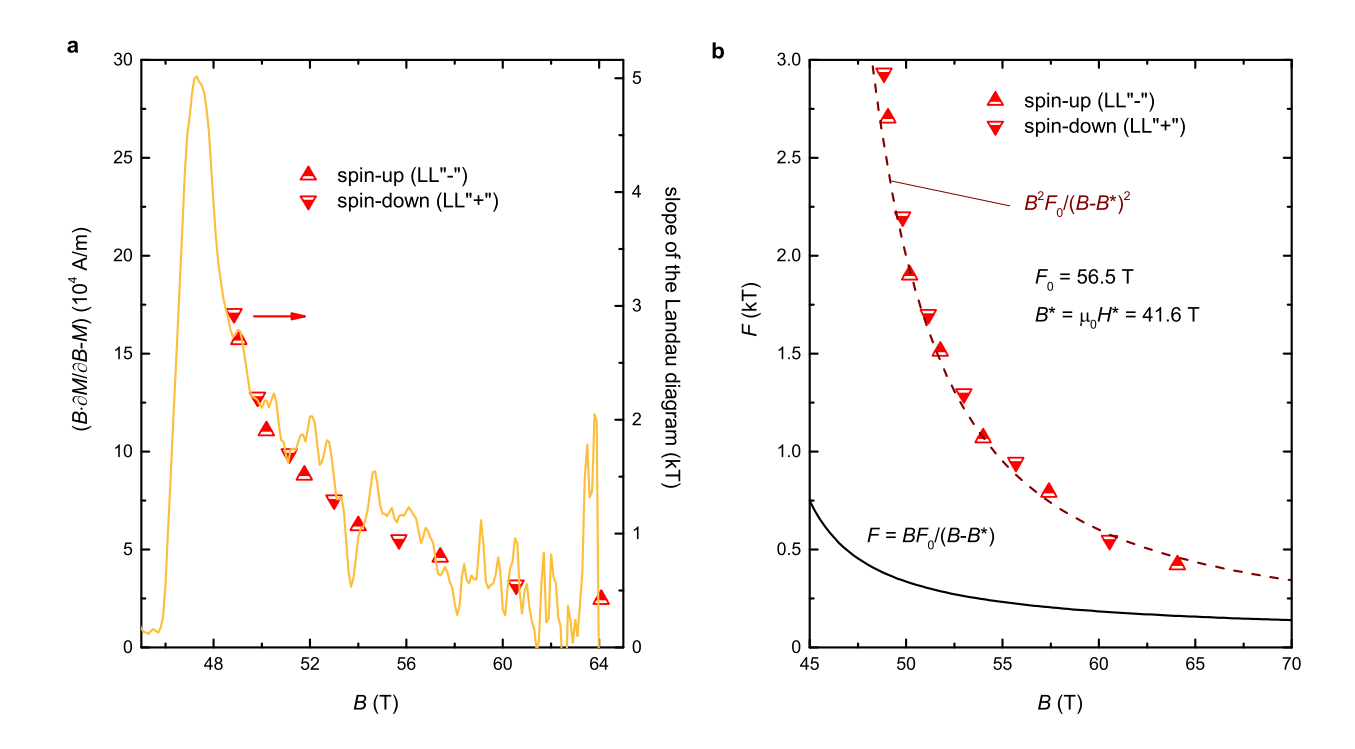


Extended Data Fig. 4. X-Ray diffraction. X-ray diffraction pattern of the YbB₁₂ single crystal measured with Cu K_{α} radiation. Only the (00*l*) series Bragg peaks are observed. The lattice parameter is calculated to be a = 7.47 Å.



Extended Data Fig. 5. The failure of the three-component model (see Supplementary Information).

a, FFT spectra of the SdH oscillations (upsweeps) shown in Extended Data Fig. 2**a**. The three apparent oscillation frequencies at small tilt angles ($\theta < 25^{\circ}$) are labelled F_1 , F_2 and F_3 , respectively. The dashed lines are a guide for the eye. **b,** FFT spectra of the SdH oscillations shown in Extended Data Fig. 2b. The cyclotron masses m_1^* , m_2^* and m_3^* are extracted from the LK fits of the T-dependent amplitudes of FFT peaks F_1 , F_2 and F_3 , respectively. **c,** The oscillatory component of PDO frequency at $\theta = -0.2^{\circ}$ (black, the same curve as shown in Fig. 1b) fitted by a three-component LK model (red). The fitting parameters F_1 , F_2 , F_3 , m_1^* , m_2^* and m_3^* are obtained from the FFT analysis exhibited in **b**. We mention that the mass differences between $\theta = -0.2^{\circ}$ and $\theta = 10.9^{\circ}$ are ignored here, since the frequency shifts are within 5%. The fit fails to capture the field dependence of the amplitude as well as the shape of the peaks in the raw data. The three components with the frequencies F_1 , F_2 and F_3 are displayed separately with a vertical offset for clarity.



Extended Data Fig. 6. The back-projected SdH frequencies in the KM state of YbB₁₂ (See Supplementary Information). a, The field dependence of the slope of the Landau diagram shown in Fig. 1c for the spin-up (up triangles) and spin-down (down triangles) branches. Both branches generally track the behaviour of $B \frac{\partial B}{\partial M} - M$, where M is the sample magnetization shown in Extended Data Fig. 1d. b, The slopes presented in a, which can be regarded as the "measured" SdH frequencies, exhibit a field dependence that can be fitted by the function $F_m(B) = F_0 B^2/(B - B^*)^2$ (deep red dashed curve), where $B^* = \mu_0 H^* = 41.6$ T and $F_0 = 56.5$ T (see Extended Data Table 1). An example "true" SdH frequency $F_{\text{orb}} = F_0 B/(B - B^*)$ is derived from the expression of $F_m(B)$ using the "back projection" approach and is denoted by the black solid curve. We emphasize that this expression for F_{orb} is exactly the same as the result of the correspondence principle, i.e., Eq. 3 (see Methods).

Extended Data Table 1. The angular dependence of F_0 (the slope of the Landau diagrams shown in Fig. 2a), the I-M transition field $\mu_0 H_{\text{I-M}}$ and the location of the PDO resonance minimum $\mu_0 H_{\text{min}}$. The values of $\mu_0 H_{\text{I-M}}$ are determined as the onset of the "dip" feature on the PDO resonance during the upsweeps shown in Fig. 1a. In this criterion, the transition field is slightly lower than that determined by the magnetization and magnetostriction measurements (see Extended Data Fig. 1c and d).

$oldsymbol{ heta}(^{\circ})$	F_0 (T)	$\mu_0 H_{\text{I-M}}$ (T)	$\mu_0 H_{\min}$ (T)
0.2	56.5±0.5	46.1	46.8
5.2	57.5±0.4	46.1	46.8
10.9	61.6±0.3	46.3	47.1
15.5	67.6±0.6	46.7	47.6
20.7	79.7±0.5	47.4	48.3